Theory of the forced wetting transition

Tak Shing Chan, Jacco H. Snoeijer, and Jens Eggers

Citation: Phys. Fluids **24**, 072104 (2012); doi: 10.1063/1.4736531
View online: http://dx.doi.org/10.1063/1.4736531
View Table of Contents: http://pof.aip.org/resource/1/PHFLE6/v24/i7
Published by the American Institute of Physics.

Theory of the forced wetting transition

Tak Shing Chan,[1] Jacco H. Snoeijer,[1] and Jens Eggers[2]
[1]*Physics of Fluids Group, Faculty of Science and Technology and Mesa+ Institute, University of Twente, P.O. Box 217, 7500 AE Enschede, The Netherlands*
[2]*Department of Mathematics - University of Bristol, University Walk, Bristol BS8 1TW, United Kingdom*

(Received 20 February 2012; accepted 26 June 2012; published online 17 July 2012)

We consider a solid plate being withdrawn from a bath of liquid which it does not wet. At low speeds, the meniscus rises below a moving contact line, leaving the rest of the plate dry. At a critical speed of withdrawal, this solution bifurcates into another branch via a saddle-node bifurcation: two branches exist below the critical speed, the lower branch is stable, the upper branch is unstable. The upper branch eventually leads to a solution corresponding to film deposition. We add the local analysis of the upper branch of the bifurcation to a previous analysis of the lower branch. We thus provide a complete description of the dynamical wetting transition in terms of matched asymptotic expansions. © *2012 American Institute of Physics*. [http://dx.doi.org/10.1063/1.4736531]

I. INTRODUCTION

Consider a partially wetting solid plate (with microscopic contact angle θ_e), being withdrawn from a liquid reservoir, as illustrated in Fig. 1. Depending on the speed of withdrawal U, two scenarios can occur. If U is above a certain threshold value U_c, a liquid film is deposited on the solid surface .[1–5] This principle is commonly used in the coating industry.[6,7] On the other hand, if $U < U_c$, an initially dry solid surface will remain dry, but the contact line position z_{cl} (see Fig. 1) rises above its equilibrium value. The critical speed is set by a balance between the liquid-gas surface tension γ and viscous forces,[8,9] which are proportional to the liquid viscosity η. As a result, the critical speed is controlled by the dimensionless *capillary number* $\mathrm{Ca} \equiv \eta U/\gamma$. For simplicity, we restrict ourselves to the most frequently used geometry of a plate being withdrawn vertically.

The bifurcation between wetted and dry states can be understood by considering the solution curve shown in Fig. 2(a), which plots z_{cl} as function of the plate speed.[10,11] Here and in the following, all lengths are scaled by the the capillary length $\ell_c \equiv \sqrt{\gamma/\rho g}$, where ρ is the fluid density and g the acceleration of gravity. Stationary solutions have been computed numerically using a modified lubrication theory,[12] which remains valid for arbitrary interface slopes. The only restriction on its validity, when compared to the full viscous fluid equations, is that of small Ca. To model the contact line motion, we introduce a microscopic slip length λ_s, which is necessary for the contact line to be able to move.[5,13] On the scale of λ_s, the interface makes a finite contact angle with the solid, which we take to be the equilibrium contact angle. More details of the modeling will be discussed below.

Below the horizontal dashed line of Fig. 2(a), the contact line position is a monotonically increasing function of speed. For very small Ca, the capillary rise approaches its equilibrium value[14]

$$z_{cl} = \sqrt{2(1 - \sin\theta_e)}. \tag{1}$$

As the speed increases, the lower branch solution ends at a maximum value Ca_c of the control parameter, which is the typical scenario for a saddle-node bifurcation.[15] At this point a transition toward a wetted state must occur, since all available steady states correspond to a smaller speed than the actual speed Ca_c. The lower branch of the solution curve corresponds to a stable equilibrium, the upper branch to an unstable equilibrium.[15] Eventually, the contact line position goes to infinity, and the plate is covered completely by a film.

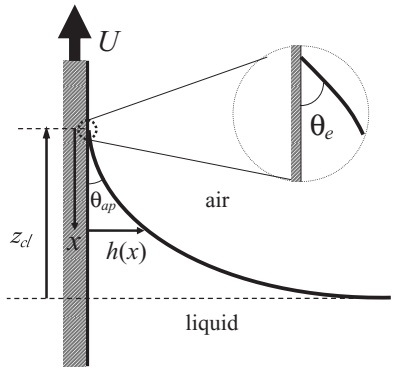

FIG. 1. Schematic diagram of a plate being withdrawn from a viscous liquid reservoir. The interface shape is $h(x)$, where x is measured relative to the contact line position: $x = z_{cl} - z$. From a large scale, the interface meets the wall with an apparent contact angle θ_{ap}. Near the contact line, the interface is highly curved, and one recovers the equilibrium contact angle θ_e at the contact line.

In Refs. 16 and 17, the lower branch of the solution curve of Fig. 2(a) has been studied analytically, using the method of matched asymptotic expansions. This approach exploits the disparity of scales between the capillary length ($\approx 10^{-3}$m), and the slip length (10^{-9}m), relevant only very close to the contact line. The outer solution is controlled by a static balance between surface tension and gravity, enabling one to use the relationship (1) between capillary rise an contact angle, but with an

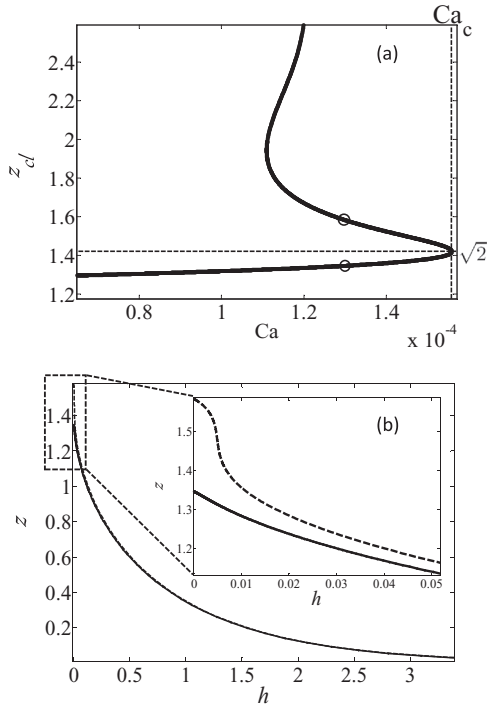

FIG. 2. (a) Bifurcation diagram of stationary solutions, showing the meniscus rise z_{cl} (in units of ℓ_c), as function of Ca for $\theta_e = 0.2$ and slip length $\lambda_s = 10^{-5}$. Solid curve: result from a numerical solution of lubrication theory, see Ref. 10. The horizontal dotted line indicates $z_{cl} = \sqrt{2}$, which is the maximum rise height of a meniscus at equilibrium. (b) Interface profiles of the lower branch solution (solid curve) and the upper branch solution (dashed curve) for Ca $= 1.3 \times 10^{-4}$ (indicated by circles in (a)). The contact line position is at $z = z_{cl}$, while $z = 0$ at the bath. In the upper branch, the interface develops a finger close to the wall, making z_{cl} much larger than expected from the extrapolation of the far-field profile.

"apparent" contact angle $\theta_{\rm ap}$,

$$z_{\rm cl} = \sqrt{2(1-\sin\theta_{\rm ap})}. \tag{2}$$

The maximum value of $z_{\rm cl}$ consistent with (2) is $z_{\rm cl} = \sqrt{2}$, which is realized for $\theta_{\rm ap} = 0$. Since (2) does not allow for solutions above $z_{\rm cl} = \sqrt{2}$, a transition occurs as the apparent contact angle vanishes. The corresponding maximum capillary number Ca_c has been calculated in Ref. 17. An inspection of Fig. 2(a) shows that the bifurcation indeed occurs very close to $z_{\rm cl} = \sqrt{2}$, and the value of Ca_c agrees quantitatively with the theoretical prediction, as well as with experiment.[10,18] An experiment withdrawing a fiber also found the transition to occur at vanishing apparent contact angle.[19]

In the present paper, we will supply the missing description of the upper branch in terms of matched asymptotic expansions. To our knowledge, this is the first time both branches of a saddle-node bifurcation have been described using this method. Matching requires a new type of inner solution, as illustrated in Fig. 2(b). We show solutions on the upper and lower branches of the transition (circles in Fig. 2(a)), but corresponding to the same value of Ca. It is clear from the main graph of Fig. 2(b) that the two solutions are virtually identical on the large scale, and thus correspond to the same value of the apparent contact angle $\theta_{\rm ap}$. However, the upper branch solution is distinguished by a different inner solution, which features a thin viscous "finger", only visible in the inset, showing a magnified region very close to the plate. As a result, the *actual* contact line position $z_{\rm cl}$ at the tip of the finger is significantly higher than $z_{\rm cl}$ obtained by extrapolating from the outer solution, and which gives $z_{\rm cl}$ on the lower branch.

The present paper is organized as follows: we first recount the technique of matched asymptotic expansion used for finding the lower branch solutions, presented in Refs. 16 and 17. We then perform an asymptotic analysis for the upper branch solutions by considering another set of inner solutions, which displays the narrow finger shape as discussed above. We thus show that on the upper branch, the true contact line position is shifted upwards from its apparent value. We demonstrate that the upper and lower branch solutions thus found can be joined at the bifurcation point. In the final discussion, we relate the bifurcation theory approach to the result of matched asymptotic expansions, and discuss remaining unsolved problems.

II. LOWER BRANCH AND CRITICAL SPEED

The lower branch of the bifurcation diagram was calculated in Ref. 17 using matched asymptotics, for the case that the angle at which the plate is withdrawn is small. In this section, we present a brief summary of this calculation, and adapt it to the case of vertical withdrawal. In the matched asymptotic description, the solution is broken up into an inner and an outer region, denoted by $h_{in}(x)$ and $h_{out}(x)$, respectively. The variable x is defined relative to the contact line position: $z = z_{cl} - x$, see Fig. 1. The full solution is found by imposing appropriate matching conditions between the two solutions.

A. Inner solution: Lubrication approximation

For simplicity, we restrict ourselves to the case of small equilibrium contact angles, $h'_{in}(0) = \theta_{\rm e} \ll 1$, so we can use the lubrication approximation close to the contact line.[5] Since the length scale in the inner region is set by the slip length λ_s, which is much smaller than ℓ_c, gravity is negligible. The corresponding lubrication equation reads[10]

$$h'''_{in} = \frac{3\mathrm{Ca}}{h_{in}^2 + 3\lambda_s h_{in}}. \tag{3}$$

Note that the presence of λ_s makes for a much weaker singularity as h_{in} vanishes. For $\lambda_s = 0$, no dynamical solution of (3) exists which makes a finite contact angle with the substrate. Thus a finite value of $\lambda_s > 0$ is needed to allow the contact line to move relative to the substrate. We scale out λ_s

from the problem, by introducing the similarity solution

$$h_{in}(x) = 3\lambda_s H\left(\frac{x\theta_e}{3\lambda_s}\right), \quad \xi = \frac{x\theta_e}{3\lambda_s}. \tag{4}$$

With these rescalings (3) can be expressed in terms of the dimensionless profile $H(\xi)$,

$$H''' = \frac{\delta}{H^2 + H}, \tag{5}$$

where we introduced a reduced capillary number $\delta = 3\mathrm{Ca}/\theta_e^3$. The boundary conditions on the plate are

$$H(0) = 0 \text{ and } H'(0) = 1. \tag{6}$$

Since (5) is a third order differential equation, one more condition is required. This condition will be obtained from the matching to the outer solution.

Away from the contact line, where $H \gg 1$, (5) further reduces to

$$y''' = \frac{1}{y^2}, \tag{7}$$

where we have put $H(\xi) = \delta^{1/3} y(\xi)$. This equation has an exact solution, whose properties have been summarized in Ref. 20. In parametric form, a solution with $y(0) = 0$ reads

$$\left.\begin{aligned} \xi &= \tfrac{2^{1/3}\pi Ai(s)}{\beta(\alpha Ai(s)+\beta Bi(s))} \\ y &= \tfrac{1}{(\alpha Ai(s)+\beta Bi(s))^2} \end{aligned}\right\} s \in [s_1, \infty[, \tag{8}$$

where Ai and Bi are the two Airy functions.[21] The limit $\xi \to 0$ corresponds to $s \to \infty$, the opposite limit $\xi \to \infty$ to $s \to s_1$, where s_1 is a root of the denominator of (8):

$$\alpha Ai(s_1) + \beta Bi(s_1) = 0. \tag{9}$$

Since the solution extends to $s = \infty$, s_1 has to be the *largest* root of (9).

The solution $y(\xi)$ is thus characterized by α, β, and s_1, but only two of these parameters are independent due to (9). As detailed in Ref. 17, the constant β can be determined by matching (8), which is valid only for $\xi \gtrsim 1$, to a solution of (5), which includes the effect of the cutoff and is thus valid down to the position $\xi = 0$ of the contact line. It was found that

$$\beta^2 = \pi \exp(-1/(3\delta))/2^{2/3} + \mathcal{O}(\delta), \tag{10}$$

which eliminates one of the remaining two free parameters. The last parameter s_1 will be eliminated below by matching the large scale asymptotics of $y(\xi)$ to the outer solution of the problem. To this end, we need the behavior of $y(\xi)$ for large ξ, which can be obtained from (8):

$$y(\xi) = \frac{1}{2}\kappa_y \xi^2 + b_y \xi + \mathcal{O}(1), \tag{11}$$

where

$$\kappa_y = \left(\frac{2^{1/6}\beta}{\pi Ai(s_1)}\right)^2, \quad b_y = \frac{-2^{2/3} Ai'(s_1)}{Ai(s_1)}. \tag{12}$$

B. Outer solution: Liquid reservoir

The outer solution $h_{out}(x)$, valid away from the contact line, is governed by a balance between surface tension and gravity:[14]

$$\kappa \equiv \frac{h''_{out}}{(1 + h'^2_{out})^{3/2}} = z_{\mathrm{cl}} - x, \tag{13}$$

where κ is the curvature of the interface. Remember that $x = 0$ at the contact line, and $x = z_{cl}$ at the height of the bath. The static balance (13) is to be solved subject to the boundary conditions

$$h_{out}(0) = 0,\ h'_{out}(0) = \theta_{\rm ap} \text{ and } h'_{out}(z_{\rm cl}) = \infty, \tag{14}$$

which contains the apparent contact angle $\theta_{\rm ap}$ as sole parameter. A Taylor expansion of the outer solution leads to

$$h_{\rm out}(x) = \tan\theta_{\rm ap} x + \frac{1}{2}\kappa_{\rm ap} x^2 + \mathcal{O}\left(x^3\right). \tag{15}$$

Integrating (13) once with respect to x, we obtain

$$1 - \frac{h'_{\rm out}}{(1 + h'^2_{\rm out})^{1/2}} = \frac{1}{2}(z_{\rm cl} - x)^2, \tag{16}$$

where the boundary condition $h'_{\rm out} \to \infty$ at the position of the reservoir ($x = z_{\rm cl}$) is used. Evaluating (16) at the contact line position ($x = 0$) and using the geometrical connection $\sin\theta = h'_{\rm out}/\sqrt{1 + h'^2_{\rm out}}$ as well as (13), we find

$$\kappa_{ap} = z_{\rm cl} = \sqrt{2(1 - \sin\theta_{ap})},$$

as quoted in the Introduction. Our main interest in this paper is the neighborhood of the bifurcation, i.e., the region of small θ_{ap}. Thus for the sake of simplicity we contend ourselves with the leading-order expressions for small θ_{ap} and find

$$h_{\rm out}(x) = \theta_{\rm ap} x + \frac{1 - \theta_{ap}/2}{\sqrt{2}} x^2 + \mathcal{O}\left(x^3\right). \tag{17}$$

C. Matching: Lower branch

To match the two solutions on the lower branch we first write the inner solution in term of the original variables,

$$h_{\rm in}(x) = \delta^{1/3}\left[\frac{\kappa_y \theta_{\rm e}^2 x^2}{6\lambda_s} + b_y \theta_{\rm e} x + \mathcal{O}(1)\right]. \tag{18}$$

Comparing this to (17), we find the matching conditions

$$\theta_{\rm ap} = \delta^{1/3} b_y \theta_{\rm e}, \tag{19}$$

$$2 - \theta_{\rm ap} = \sqrt{2}\delta^{1/3}\frac{\kappa_y \theta_{\rm e}^2}{3\lambda_s}. \tag{20}$$

Adding these two conditions leads to an equation for s_1 as a function of δ:

$$\frac{2}{\theta_{\rm e}\delta^{1/3}} + \frac{2^{2/3} Ai'(s_1)}{Ai(s_1)} = \frac{2^{1/6}\exp[-1/(3\delta)]}{3\pi\, Ai^2(s_1)\lambda_s/\theta_{\rm e}}. \tag{21}$$

Once s_1 is known, one can compute the apparent contact angle

$$\frac{\theta_{\rm ap}}{\theta_{\rm e}} = -\frac{2^{2/3}\delta^{1/3} Ai'(s_1)}{Ai(s_1)}. \tag{22}$$

Analysis of (21) shows[17] that solutions cease to exist above a critical reduced speed δ_c, for which the apparent contact angle goes to zero. According to (22), this occurs when the Airy function takes its global maximum, $Ai'(s_1) = 0$, corresponding to $s_{\rm max} = -1.088\cdots$ (cf. Fig. 3). This gives a critical speed

$$\delta_c = \frac{1}{3}\left[\ln\left(\frac{\delta_c^{1/3}\theta_{\rm e}^2}{2^{5/6} 3\pi (Ai(s_{\rm max}))^2 \lambda_s}\right)\right]^{-1}; \tag{23}$$

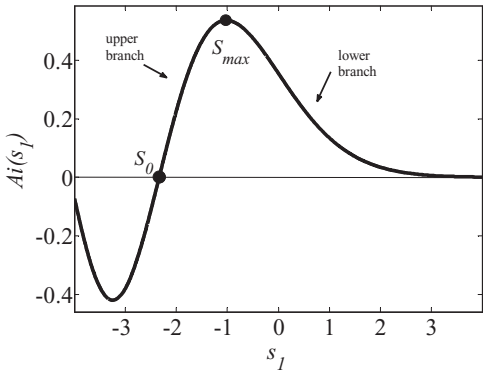

FIG. 3. Airy function $Ai(s_1)$. The critical point occurs at $s_{\max} = -1.088\cdots$ where the Airy function takes its maximum value. The lower and upper branches of the bifurcation diagram correspond to $s_1 \geq s_{\max}$ and $s_0 < s_1 < s_{\max}$, respectively, where $s_0 = -2.338\cdots$ is the rightmost zero of $Ai(s_1)$.

remember that δ_c is related to the critical capillary number by $\mathrm{Ca_c} = \delta_c \theta_e^3/3$. This completes the description of the lower branch of Fig. 2(a), up to the critical capillary number. However, the analysis so far gives no clue as to what happens beyond the transition, and thus does not explain the nature of the transition.

III. UPPER BRANCH AND BIFURCATION DIAGRAM

We now turn to the upper branch of the bifurcation diagram close to the critical speed. Clearly, this branch cannot be described in terms of (2), since z_{cl} rises above the maximum value of $\sqrt{2}$ corresponding to $\theta_{\mathrm{ap}} = 0$. The critical point is attained when $Ai(s_1)$ takes its maximum value, at $s_1 = s_{\max} = -1.088\cdots$ (cf. Fig. 3). The rest of the lower branch corresponds to values $s_1 > s_{\max}$. This suggests that the upper branch can be described in terms of solutions on the other side of the maximum, $s_1 < s_{\max}$, and below we will work out this idea.

A. Matching: Upper branch

An inspection of (12) shows that b_y is strictly negative in the domain $s_0 < s_1 < s_{\max}$, where $s_0 = -2.338\cdots$ is the rightmost zero of the Airy function (cf. Fig. 3). Thus we cannot impose the same matching as in Sec. II, since (19) would imply a negative apparent contact angle. We get around this problem by noting that the large scale asymptotics of the inner solution (11) is a parabola that has two zeros, $\xi = 0$ and $-2b_y/\kappa_y$. The former coincides with the actual position of the contact line, while we interpret the latter as the "apparent" position of the contact line

$$\xi_{\mathrm{ap}} = \frac{-2b_y}{\kappa_y}. \tag{24}$$

Figure 4 illustrates how a typical solution (8) (solid line) approaches its asymptotic limit (11) (dashed line), so that the *relative* distance between the two curves goes to zero for large ξ. Matching the next (constant) term in (11) would be achieved only at the next order of the asymptotic expansion. Extrapolating the large-scale solution to the plate position, the contact line appears to be located at $\xi = \xi_{ap}$, while its actual position is at $\xi = 0$. This is due to the narrow finger exhibited by solutions $y(\xi)$ for the parameter range $s_0 < s_1 < s_{\max}$ (cf. inset of Fig. 4). This finger was already visible in the numerical solutions shown in Fig. 2(b).

Expanding (11) relative to the apparent contact line position ξ_{ap}, we obtain

$$\begin{aligned} y(\xi) &= \frac{1}{2}\kappa_y \xi^2 + b_y \xi + \mathcal{O}(1) \\ &= \frac{1}{2}\kappa_y \left(\xi - \xi_{\mathrm{ap}}\right)^2 - b_y \left(\xi - \xi_{\mathrm{ap}}\right) + \mathcal{O}(1). \end{aligned} \tag{25}$$

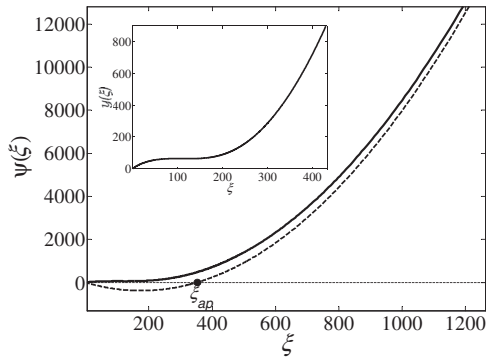

FIG. 4. The profile (8) for $s_1 = -2.0$ and $\delta = 0.063$ (solid line). The dashed line is the asymptotic form (11) of the profile for large ξ; from a large scale, the contact line appears to be located at $\xi_{\rm ap} \sim 350$. The inset is a zoom on the contact line region showing a narrow finger which ends at the contact line $\xi = 0$.

The prefactor of the linear term, $-b_y$, is now strictly positive on $s_0 < s_1 < s_{\max}$ and can therefore be matched to a "shifted" bath solution:

$$h_{\rm out}(x) = \theta_{\rm ap}\left(x - x_{\rm ap}\right) + \frac{1 - \theta_{ap}/2}{\sqrt{2}}\left(x - x_{\rm ap}\right)^2 + \mathcal{O}\left((x - x_{\rm ap})^3\right). \tag{26}$$

Retracing the steps of Sec. II, one finds the equation for s_1 as

$$\frac{2}{\theta_{\rm e}\delta^{1/3}} - \frac{2^{2/3}Ai'(s_1)}{Ai(s_1)} = \frac{2^{1/6}\exp[-1/(3\delta)]}{3\pi\, Ai^2(s_1)\lambda_s/\theta_{\rm e}}. \tag{27}$$

This differs from (21) only by a minus sign in the second term of the left-hand side. Similarly, the apparent contact angle follows as

$$\frac{\theta_{\rm ap}}{\theta_{\rm e}} = \frac{2^{2/3}\delta^{1/3}Ai'(s_1)}{Ai(s_1)}, \tag{28}$$

with a change in sign. In Fig. 5, we plot θ_{ap} as function of δ for both lower branch (solid line) and upper branch (dotted line). Both curves meet at $\delta = \delta_c$, where the apparent contact angle vanishes. Thus the apparent contact angle decreases as the transition is approached from below, and then increases again on the upper branch.

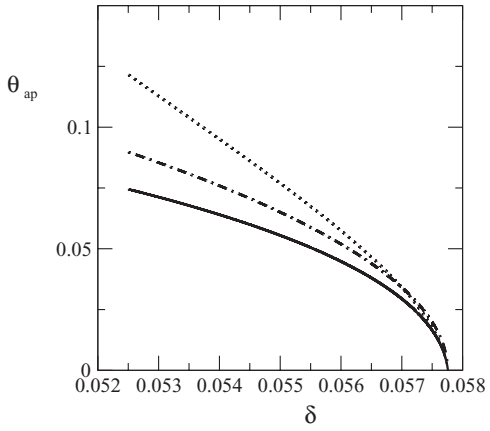

FIG. 5. The apparent contact angle θ_{ap} as function of δ for lower branch (solid line) and upper branch (dotted line). The two curves meet at $\delta = \delta_c \approx 0.0578$, where $\theta_{ap} = 0$. The dot-dashed line corresponds to (37) below.

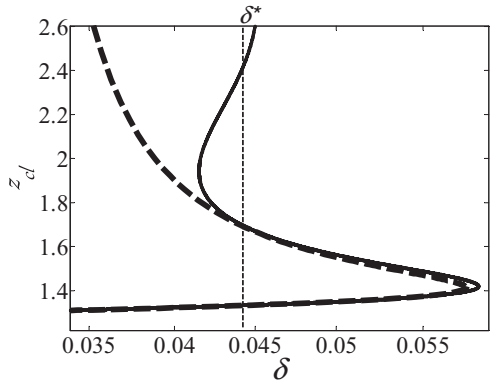

FIG. 6. Meniscus rise $z_{\rm cl}$ as function of δ for $\theta_{\rm e} = 0.2$ and the slip length $\lambda_s = 10^{-5}$. Solid line: Same as in Fig. 2(a). Dashed lines are (31), with θ_{ap} from (21) and (22) (lower branch) and (27) and (28) (upper branch). For large z_{cl}, the curve approaches a limiting speed δ^*.

B. Meniscus rise

Let us now express the new solution in terms of the meniscus rise $z_{\rm cl}$ and compare to the bifurcation diagram of Fig. 2(a). To do so, we need to take into account the difference between the real position of the contact line at $\xi = 0$, and the apparent position $\xi_{\rm ap}$. This difference comes on top of the meniscus rise of the outer solution, given by (2), so that in original variables

$$z_{\rm cl} = \sqrt{2}(1 - \theta_{\rm ap}/2) + \xi_{\rm ap}\frac{3\lambda_s}{\theta_{\rm e}}, \tag{29}$$

once more expanding for small $\theta_{\rm ap}$. Rewriting (25) in terms of the outer variables x and h, and comparing it to (26), we obtain

$$b_y = \frac{-\theta_{ap}}{\delta^{1/3}}, \quad \kappa_y = \frac{3\cdot\sqrt{2}\lambda_s}{\delta^{1/3}\theta_e}.$$

Now using (24), one finds

$$\xi_{\rm ap}\frac{3\lambda_s}{\theta_{\rm e}} = \sqrt{2}\theta_{\rm ap}, \tag{30}$$

giving the contact line position directly in terms of $\theta_{\rm ap}$. Thus we finally arrive at

$$z_{\rm cl} = \sqrt{2}\begin{cases} 1 - \theta_{\rm ap}/2 & \text{for} \quad z_{\rm cl} \le \sqrt{2} \\ 1 + \theta_{\rm ap}/2 & \text{for} \quad z_{\rm cl} \ge \sqrt{2}. \end{cases} \tag{31}$$

To test (31), in Fig. 6 we replot $z_{\rm cl}$ as function of δ for the same parameter values as those of Fig. 2(a). The solid curve is the numerical solution of the improved lubrication theory, the dashed lines represent (31), with θ_{ap} calculated for the lower and upper branches, respectively. The agreement of the numerical result and the analytical results is very good for both branches.

C. Comparison to bifurcation theory

Returning to the bifurcation argument presented in the Introduction, the transition occurs because the solution curve folds over, and is thus guaranteed to have a local expansion of the form

$$\delta - \delta_c = a_1\left(z_{\rm cl} - \sqrt{2}\right)^2 + \mathcal{O}\left(z_{\rm cl} - \sqrt{2}\right)^3. \tag{32}$$

To discover the local behavior resulting from the matched asymptotics, we insert the expansion

$$\delta - \delta_c = \delta_1\delta s_1 + \delta_2\delta s_1^2, \quad \delta s_1 = s_1 - s_{\rm max} \tag{33}$$

into (21) and (27), respectively. On the basis of (32), we would expect δ_1 to vanish and δ_2 to be the same above and below the transition.

Instead, we find

$$\delta_1 = -\frac{3\sigma 2^{2/3} s_{\max} \theta_e \delta_c^{7/3}}{2(\delta_c + 1)}, \tag{34}$$

where $\sigma = \pm 1$ above and below the transition, respectively; the coefficient δ_2 does not have a definite sign. Clearly, the bifurcation curve as predicted by matched asymptotics is *not* smooth at the bifurcation point. Indeed, close inspection of Fig. 6 reveals that the dashed line does not have a vertical tangent at the turning bifurcation point.[17] Instead, the "correct" behavior emerges only in the limit of small slip length $\lambda_s \to 0$ or $\delta_c \to 0$. In this limit, we find

$$\delta_2 = 3 s_{\max} \delta_c^2, \tag{35}$$

which is indeed the same above and below the transition. Thus the first term of (33) is negligible (and the structure (32) is valid) for $\delta s_1 \gg \delta_c^{1/3}$.

In addition, from (22) and (28) we find that to leading order

$$\theta_{ap} = -2^{2/3} \theta_e s_{\max} \delta_c \, |\delta s_1| \,, \tag{36}$$

which is valid both above ($\delta s_1 < 0$) and below ($\delta s_1 > 0$) the transition. Thus in summary we find

$$\theta_{ap} = 2^{2/3} \theta_e \left| \frac{s_{\max}}{3} \right|^{1/2} \delta_c^{-2/3} \, |\delta - \delta_c|^{1/2} \,, \tag{37}$$

which is valid for $\theta_{ap} \gg \delta_c^{2/3}$. The asymptotic local behavior (37) is plotted in Fig. 5 as the dot-dashed line. Its behavior for small θ_{ap} is hard to distinguish from (22) and (28).

IV. DISCUSSION

Matched asymptotics clearly gives a quantitative description of both branches of the saddle-node bifurcation. In the case of the lower branch, this holds true for the entire branch down to vanishing speed. The behavior of the upper branch, on the other hand, is considerably more complicated, as described in Refs. 4 and 18. Following the upper branch, one encounters an infinite sequence of saddle-node bifurcations, as the solution curve oscillates around a second characteristic speed δ^*. The oscillations of the solution curve, which are due to oscillations of the interface profile,[22] are damped very quickly, so at a capillary rise of a few times the capillary length the solution effectively corresponds to a film of constant thickness covering the plate. This film, of thickness $h^* = \sqrt{\delta^* \theta_e^3}$, is maintained by a balance of viscosity and gravity. Experimentally, this film has indeed been realized when a plate is withdrawn with speed above δ^*.[4]

Our present analysis is not able to capture this feature, since gravity is not included in the balance (3), which describes the inner solution. As the finger seen in the inset of Fig. 4 grows in length, the hydrostatic pressure difference across it becomes significant, and the solution fails. An estimate of the capillary rise at which this occurs is obtained from the intersection between (31) and the vertical line δ^*, along which gravity and viscosity balance. Using (31) and (37), this leads to the estimate

$$z_{\mathrm{cl}} - \sqrt{2} \approx \theta_e \delta_c^{-2/3} \sqrt{\delta_c - \delta^*} \tag{38}$$

for the rise at which gravity becomes significant. Using $\delta_c \approx 0.058$ and $\delta^* \approx 0.044$, this leads to $z_{\mathrm{cl}} - \sqrt{2} \approx 0.16$, which agrees reasonably well with Fig. 6.

It is worth reviewing the relative merits of bifurcation theory and those of matched asymptotics, which are complementary. Within bifurcation theory, once one understands the origin of the transition as a fold of the solution curve of Fig. 2(a), the local structure or order of the transition results automatically. In addition, it is clear that the transition must correspond to moving from a stable branch to an unstable branch.[15] As always, the disadvantage is that the critical parameters of the transition, such as δ_c, cannot be calculated within bifurcation theory.

Matched asymptotics, on the other hand, requires a detailed calculation, which reveals the full spatial structure of the solution above and below the transition, as well as the values of all the critical parameters, calculated directly from the system parameters. For example, it is shown that the upper branch solution contains an additional, and unforseen structure, which is the finger seen in Fig. 2(b). However, the local structure (32) of the saddle-node bifurcation emerges from the calculation only in the limit $\lambda_s \to 0$ or $\delta_c \to 0$. Note the subtle point that the two branches as predicted by asymptotics do not fit together to form a differentiable curve. The reason is that both parts present very different spatial features, and hence agreement between matched asymptotic expansion and bifurcation theory is achieved in a pointwise fashion only. It would be an interesting project to see if the next order of the asymptotic expansion will reproduce the next term in the expansion about the bifurcation point.

The stability properties of the two branches have not yet been investigated within matched asymptotics, and remain a non-trivial problem: the task is to properly separate the timescales of the inner and outer solutions. The result is expected to be an effective dynamics,[10] in which the solution moves quasi-statically along the solution curve. This picture of quasi-steady dynamics was confirmed in experiments where the plate velocity was taken above the critical speed.[18] It was found that during the deposition of the liquid film, the upward motion of the contact line follows the bifurcation curve perfectly when replacing the plate velocity by the relative velocity of the contact line, i.e., $U - dz_{cl}/dt$.

In conclusion, we have calculated the upper and lower branches of a saddle-node bifurcation using matched asymptotics. We are not aware of any other example of this having been done before. It would be of great interest to develop a more general framework of correspondences between certain types of bifurcations, and the matched asymptotics needed to describe them.

ACKNOWLEDGMENTS

T.S.C. acknowledges financial support by the FP7 Marie Curie Initial Training Network Surface Physics for Advanced Manufacturing project ITN 215723.

[1] B. V. Deryaguin and S. M. Levi, *Film Coating Theory* (Focal, London, 1964).
[2] T. D. Blake and K. J. Ruschak, "A maximum speed of wetting," Nature (London) **282**, 489–491 (1979).
[3] J. H. Snoeijer, G. Delon, M. Fermigier, and B. Andreotti, "Avoided critical behavior in dynamically forced wetting," Phys. Rev. Lett. **96**, 174504 (2006).
[4] J. H. Snoeijer, J. Ziegler, B. Andreotti, M. Fermigier, and J. Eggers, "Thick films coating a plate withdrawn from a bath," Phys. Rev. Lett. **100**, 244502 (2008).
[5] D. Bonn, J. Eggers, J. Indekeu, J. Meunier, and E. Rolley, "Wetting and spreading," Rev. Mod. Phys. **81**, 739 (2009).
[6] D. Quéré, "Fluid coating on a fiber," Annu. Rev. Fluid Mech. **31**, 347 (1999).
[7] S. J. Weinstein and K. J. Ruschak, "Coating flows," Annu. Rev. Fluid Mech. **36**, 29–53 (2004).
[8] O. V. Voinov, "Hydrodynamics of wetting," Fluid Dyn. **11**, 714–721 (1976).
[9] R. G. Cox, "The dynamics of the spreading of liquids on a solid surface. Part 1. Viscous flow," J. Fluid Mech. **168**, 169–194 (1986).
[10] J. H. Snoeijer, B. Andreotti, G. Delon, and M. Fermigier, "Relaxation of a dewetting contact line. Part 1. A full-scale hydrodynamic calculation," J. Fluid Mech. **579**, 63 (2007).
[11] T. S. Chan, T. Gueudré, and J. H. Snoeijer, "Maximum speed of dewetting on a fiber," Phys. Fluids **23**, 112103 (2011).
[12] J. H. Snoeijer, "Free-surface flows with large slopes: Beyond lubrication theory," Phys. Fluids **18**, 021701 (2006).
[13] C. Huh and L. E. Scriven, "Hydrodynamic model of steady movement of a solid/liquid/fluid contact line," J. Colloid Interface Sci. **35**, 85–101 (1971).
[14] L. D. Landau and E. M. Lifshitz, *Fluid Mechanics* (Pergamon: Oxford, 1984).
[15] Drazin, *Nonlinear Systems* (Cambridge University Press, Cambridge, 1992).
[16] J. Eggers, "Hydrodynamic theory of forced dewetting," Phys. Rev. Lett. **93**, 094502 (2004).
[17] J. Eggers, "Existence of receding and advancing contact lines," Phys. Fluids **17**, 082106 (2005).
[18] G. Delon, M. Fermigier, J. H. Snoeijer, and B. Andreotti, "Relaxation of a dewetting contact line. Part 2. Experiments," J. Fluid Mech. **604**, 55 (2008).
[19] R. V. Sedev and J. G. Petrov, "The critical condition for transition from steady wetting to film entrainment," Colloids Surf. **53**, 147 (1991).
[20] B. R. Duffy and S. K. Wilson, "A third-order differential equation arising in thin-film flows and relevant to Tanner's law," Appl. Math. Lett. **10**, 63 (1997).
[21] M. Abramowitz and I. A. Stegun, *Handbook of Mathematical Functions* (Dover, 1968).
[22] J. Ziegler, J. H. Snoeijer, and J. Eggers, "Film transitions of receding contact lines," Eur. Phys. J. Spec. Top. **166**, 177 (2009).